A Diffuse-Interface Description of Internal Waves in a Near-Critical Fluid

D. M. Anderson
and
G. B. McFadden

Mathematical and Computational Sciences Division
National Institute of Standards and Technology
Gaithersburg, MD 20899, USA
tel: (301) 975–4333, fax: (301) 990–4127

March 12, 1997

Abstract

We present a diffuse-interface treatment of the internal gravity waves which have been observed experimentally by Berg *et al.* in xenon near its thermodynamic critical point. The results are compared with theoretical predictions by Berg *et al.* that were obtained using separate models above and below the critical temperature T_c. The diffuse-interface model applies both above and below T_c, and is formulated by using the density as an order parameter. The diffuse interface is represented as a transition zone of rapid but smooth density variation in the model, and density gradients appear in a capillary tensor, or Korteweg stress term, in the momentum equation. We obtain static density profiles, compute internal wave frequencies and compare with the experimental data and theoretical results of Berg *et al.* both above and below the critical temperature. The results reveal a singularity in the diffuse-interface model in the limit of incompressible perturbations.

1. Introduction

The singular behavior of the material properties of a liquid-vapor system near the thermodynamic critical point [1] leads to a number of interesting fluid phenomena. The critical point is characterized by definite values of the temperature, T_c, pressure, P_c, and density, ρ_c, that depend on the specific material under consideration. Several bulk equilibrium properties, such as specific heat and isothermal compressibility, exhibit values that diverge at the critical point, with characteristic exponents that do not depend on the specific material. The accurate determination of these critical-point exponents is a subject of considerable experimental and theoretical study. Transport properties, such as the shear and bulk viscosities and thermal conductivity, also show singular behavior near the critical point. In addition, as the temperature of a liquid-vapor system is raised to just below T_c, the liquid-vapor interface becomes increasingly diffuse, a phenomena that is related to the scattering of visible light ("critical opalescence") from micron-scale structures in the fluid.

The large increase in compressibility near the critical point leads to significant density stratification in terrestrial gravity levels, resulting in sample inhomogeneities that complicate the accurate experimental determination of critical-point exponents on earth [2,3]. For xenon in 1 g, for example [4], the density variation just above the critical point can be as much as 10 % in 1 cm. Experiments in a microgravity environment allow temperatures much closer to T_c to be considered without encountering significant density stratification.

An interesting consequence of the density stratification near the critical point in 1 g is the occurrence of internal waves in a centimeter-scale system [5–7]. These waves have been observed during experiments designed to measure the shear viscosity of xenon near the critical point [4]. The experimental procedure is based on a simultaneous measurement of the torque and displacement amplitude of an oscillating wire mesh paddle that is immersed in the fluid, from which the shear viscosity of the fluid can be inferred. In certain frequency ranges, the forced oscillation of the paddle is found to trigger internal wave modes with frequencies on the order of 1 Hz. These modes are an undesirable feature of the measurement process in 1 g, but are not expected to interfere with measurements in microgravity. On the other hand, the critical viscometer serves as a very sensitive detector of internal waves in 1 g, allowing their observation in laboratory-scale systems under well-controlled conditions.

In previous work [4], a theoretical analysis of the predicted frequencies of internal waves was based on two separate models that were applied either above or below the critical temperature. A restricted cubic model [8] for the thermodynamics of the near-critical fluid was used to compute the equilibrium density profile, which was then used in a numerical determination of the internal wave frequencies. In the one-phase regime ($T > T_c$), this resulted in a single two-point boundary problem for the amplitude and frequency of the wave motion, with boundary conditions applied at the horizontal walls of the sample. In the two-phase regime ($T < T_c$), governing equations were posed separately in the liquid and vapor regions. The liquid-vapor interface was assumed to be sharp, and standard jump conditions on the pressure and flow velocities were applied there.

In the present work we recompute the internal wave frequencies by using a single model for both the one-phase and two-phase regimes that is based on a diffuse-interface treatment of the liquid-vapor system. The model we employ is based on a thermodynamic formulation of the problem that includes contributions from a gradient-energy term [9] that lead to localized but smooth transitions at phase boundaries. The gradient energy term leads to a capillary tensor that appears in the momentum equation, making local contributions in the transition layer that represents the diffuse liquid-vapor interface. Given the diffuse nature of the actual liquid-vapor interface near the critical point, such a model is a natural candidate for a unified treatment of wave motion in a near-critical fluid. In this model, the width of the diffuse interface varies with temperature, being narrow for $T \ll T_c$, becoming increasingly diffuse at temperatures near T_c, and leading to a single-phase system for $T \gg T_c$.

Diffuse-interface models of this general type are common in mean-field approximations to finer-scale (atomic-level) descriptions of phase transitions (see, e.g., Chaikin & Lubensky

[10]). Diffuse-interface treatments without convection have been employed to describe a number of phase transitions, such as in liquid-liquid systems [11], solid-liquid systems [12–17], and solid-solid systems [18, 19]. Models that include the effects of fluid flow have also been studied [20–39], and are a current area of research. There are related fluid flow models derived from a more computational point of view that employ a numerically-diffuse description of the interface and, for example, represent the surface tension as a volumetric force in order to use a single domain approach to compute the flow [40–42]. In the level set approach [43], the interface is represented as a level set of a smooth auxiliary function which is in some ways analogous to the order parameter functions that are used in diffuse-interface descriptions. An advantage of the level set method is that the interface remains sharp in this formulation, which eliminates the need for added numerical resolution in the direction normal to the interface. In contrast to these numerical approaches, the diffuse nature of the interface in the present work arises as a result of the physical model, rather than the numerical approach. Further, in other instances such as phase-field models of solidification, the physical interpretation of the order parameter used in the gradient energy term can be unclear. In the present work the fluid density itself is used as the order parameter, and the diffuse interface is represented as a transition region of rapid but smooth density variation.

The present diffuse-interface approach, which applies both above and below the critical temperature, shall be compared with the experimental and theoretical results of Berg *et al.* [4] in order to assess the quantitative capabilities of the diffuse-interface model. For convenience, we shall use a simpler equation of state, which allows an analytical solution for the density profile, rather than the more accurate but complicated restricted cubic model used by Berg *et al.* The present equation of state can be implemented easily in both the diffuse-interface model and the sharp-interface model allowing for a direct comparison between the two models to be made.

In section 2 we describe the diffuse-interface model for the compressible, adiabatic motion of a single-component fluid near its critical point. In section 3 we outline the configuration used by Berg *et al.* [4] to study internal gravity waves in near-critical xenon and obtain static density profiles using an approximate van der Waals equation of state. Then, we compute internal gravity wave frequencies associated with these profiles and compare with the results of Berg *et al.* Results are discussed in section 4 and conclusions are given in section 5.

2. Formulation

The hydrodynamic equations governing inviscid, compressible flow of a single-component fluid near its critical point are described by conservation equations for mass, momentum, and entropy (energy),

$$\frac{D\rho}{Dt} = -\rho\nabla\cdot\vec{u}, \tag{1a}$$

$$\rho\frac{D\vec{u}}{Dt} = -\nabla p - \rho g\hat{z} + K\nabla\cdot\boldsymbol{T}, \tag{1b}$$

$$\frac{Ds}{Dt} = 0, \tag{1c}$$

where $D/Dt = \partial/\partial t + \vec{u}\cdot\nabla$ is the material derivative, ρ is the fluid density, $\vec{u}$ is the three-dimensional fluid velocity with components (u, v, w), $s(T,\rho)$ and $p(T,\rho)$ are the entropy per unit mass and the pressure, respectively (specified by an appropriate equation of state), T is the temperature, g is the gravitational acceleration, $\hat{z}$ is the unit normal in the vertical direction, K is the gradient energy coefficient which for simplicity we assume to be constant, and $\boldsymbol{T}$ is the capillary tensor given by

$$\boldsymbol{T} = \left(\rho\nabla^2\rho + \frac{1}{2}|\nabla\rho|^2\right)\boldsymbol{I} - \nabla\rho\otimes\nabla\rho, \tag{2}$$

where $\boldsymbol{I}$ is the identity matrix and $\otimes$ is the tensor (outer) product. Note that

$$\nabla\cdot\boldsymbol{T} = \rho\nabla(\nabla^2\rho). \tag{3}$$

Equations of this form have been considered by a number of authors (e.g. Fixman [20], Felderhof [21], Langer and Turski [23], de Sobrino [25], Dunn and Serrin [30], Jacqmin [36], Seppecher [37] and Nadiga and Zaleski [38]). The thrust of much of this work has been towards applications in which capillarity was a dominant mechanism in the dynamics. In our case, capillarity, though generally present, is a small factor in the momentum balance, since the surface tension vanishes at the critical point where the liquid and vapor phases become indistinguishable. The diffuse nature of the interface in our case, however, is still of central importance.

The capillary tensor $\boldsymbol{T}$ in the momentum equation is based on the density ρ and its gradients. It is also possible to formulate descriptions in which the momentum equation has the same form as above, but the capillary tensor is based on an auxiliary conserved order parameter (such as the composition in a binary fluid) rather than the density [31–36, 39]. In contrast to these cases, the interface in the present model is described directly in terms of the density, and the capillary terms are based on density gradients rather than gradients of the conserved order parameter. This results in a smaller set of equations, since it is then unnecessary to augment the equations by coupling them to a Cahn-Hilliard equation for the conserved order parameter; the density is governed by the usual continuity equation.

Korteweg [44] was the first to use a capillary tensor (2) to describe capillary effects of a diffuse interface. A review by Davis and Scriven [45] describes a number of alternative approaches to deriving the equilibrium stress in inhomogeneous fluids and results similar to equation (2). More general forms than the one used here and derivations based on mechanical theories have been given (e.g. Aifantis and Serrin [46, 47]).

The key difference between these equations and the sharp-interface equations describing a two-fluid system is the presence of a capillary tensor $\boldsymbol{T}$ which models capillary forces associated with the interface. The presence of this term allows these equations to apply over the entire domain, including the interfacial region; no interfacial conditions are required. Boundary conditions applied at container walls, for example, are required. These shall be discussed more thoroughly as needed for the present work. The intersection of the diffuse interface and a container boundary is, in general, a moving contact line and is not treated here but has been addressed by Cahn [48], Brackbill *et al.* [40], Jacqmin [36] and Seppecher

[37].

The nonclassical capillary term appearing in the momentum equation can be understood by relating equations (1) to global quantities and balance laws. We define the mass M, energy E and entropy S in a material subvolume $\Omega(t)$ of the total volume $\mathcal{V}$ by

$$M = \int_{\Omega(t)} \rho dV, \tag{4a}$$

$$E = \int_{\Omega(t)} \left(\frac{1}{2}\rho|\vec{u}|^2 + \rho g z + \rho e(s,\rho) + \frac{1}{2}K|\nabla\rho|^2\right) dV, \tag{4b}$$

$$S = \int_{\Omega(t)} \rho s dV. \tag{4c}$$

The total mass is given simply by the integral over the local density. The total energy is composed of classical and nonclassical contributions. The classical terms include kinetic energy, gravitational potential energy and internal energy $e(s,\rho)$ given per unit mass. The nonclassical term is in the form of a gradient energy associated with steep variations in density [9]. This nonclassical term represents an energy excess associated with the interfacial region. Consistent with a constant gradient energy coefficient in equation (4b) there is no gradient entropy term [49, 50] in equation (4c).

The governing equations (1) are consistent with the balance laws

$$\frac{dM}{dt} = 0, \tag{5a}$$

$$\frac{dE}{dt} = \int_{\delta\Omega(t)} \left(-p\vec{u}\cdot\hat{n} + K\hat{n}\cdot\boldsymbol{T}\cdot\vec{u} + K\frac{D\rho}{Dt}\nabla\rho\cdot\hat{n}\right) dA, \tag{5b}$$

$$\frac{dS}{dt} = 0, \tag{5c}$$

where $\delta\Omega(t)$ is the boundary of the subvolume and $\hat{n}$ is its outward normal. The first balance law (5a) states that mass is conserved. The second balance law (5b) states that the change in the energy of the subvolume is associated with the rate of (reversible) work done by pressure and capillary forces on the boundary as well as a nonclassical flux of stored energy in the interface. Note that this flux term is associated with compression of the flow in the interfacial region. Dunn and Serrin [30] noted that this term was a necessary part of the thermodynamic description when the Korteweg capillary tensor was present and referred to this flux as the interstitial working. Wang *et al.* [14] identified a similar nonclassical entropy flux term (without the advective term) in their phase-field model of solidification (see their equation (6)) and identified it as an entropy flux associated with variations in the phase-field at the boundary of the subvolume. The third balance law (5c) states that the change in total entropy in the subvolume $\Omega(t)$ is conserved (i.e. zero entropy production). The above model does not include dissipative effects but these can be incorporated in a straightforward way [50].

3. Internal Gravity Waves

In the experiments of Berg *et al.* [4], a mesh paddle inside a small container of near-critical xenon was driven at a fixed frequency, stopped, and then residual internal wave frequencies were measured. This was done for a range of temperatures, both above and below the critical temperature. For a horizontally-oriented cell (i.e. the paddle rotates about a vertical axis, see figure 1), which is the case we shall consider here, they observed two distinct internal gravity wave modes whose frequencies were temperature dependent. The higher frequency mode had relatively large amplitude disturbances near the horizontal mid-plane of the cell, while the lower frequency mode had relatively little motion near the mid-plane of the cell.

They modeled these waves using two separate hydrodynamic models. One model applied in the single-phase region (above the critical temperature) and another applied in the two-phase region (below the critical temperature). They used as their equation of state the restricted cubic model [3, 8], which gave a very accurate description of the static density profiles as the temperature varied. Their theoretical predictions for the internal gravity wave frequencies agreed well with those observed experimentally.

The model configuration consists of a rectangular cell with dimensions $0 \leq x \leq a_x$, $0 \leq y \leq a_y$ and $-L \leq z \leq L$ where gravity is in the $-z$ direction (see figure 1). Note that no paddle is present in the mathematical model. The physical dimensions used by Berg *et al.* correspond to $a_x = 7.6\text{mm}$, $a_y = 38\text{mm}$ and $L = 9.5\text{mm}$. These values will be used exclusively here. The results of Berg *et al.* indicate that while this geometry is a simplification of the actual internal geometry of the cell used in the experiments, it is a reasonable approximation in terms of identifying the internal wave modes and frequencies.

We shall model the motion of the fluid in this cell with the diffuse-interface approach described in section 2. We first seek static density profiles (vertical stratification and no flow) using an approximate van der Waals equation of state and then perturb these density profiles to identify the associated natural internal wave frequencies. We shall compare the present results with the theoretical predictions (for both the restricted cubic model and the van der Waals equation of state) and the experimental data of Berg *et al.*

3.1 Basic-State Density Profiles

The steady basic-state solution, denoted by subscript '0', has zero flow, is isothermal and horizontally uniform, and satisfies

$$\frac{dp_0}{dz} = -\rho_0 g + K\rho_0 \frac{d^3\rho_0}{dz^3}. \tag{6}$$

This equation determines the static density profile when an equation of state $p = p(T, \rho)$ is given. It will be useful to work with a free energy so we employ the thermodynamic relation

$$p = \rho^2 \frac{\partial f}{\partial \rho}\bigg|_T, \tag{7}$$

where f is the Helmholtz free energy per unit mass. Integrating equation (6) then gives

$$K\frac{d^2\rho_0}{dz^2} = \frac{\partial(\rho f)}{\partial \rho} + gz + c_0, \tag{8}$$

where c_0 is a constant of integration. An equivalent derivation of equation (8) involves minimizing the total energy E (equation (4b)) subject to constant total entropy S (equation (4c)) and constant total mass M (equation (4a)) over the total volume $\mathcal{V}$ for the case of no flow. Note that in order to focus on the critical point, we have assumed that the average density is equal to the critical density ρ_c so that M takes on the fixed value $\rho_c\mathcal{V}$.

We shall consider a classical van der Waals equation of state (e.g. Stanley [1], Callen [51]) as a reasonable starting point for our analysis. Despite its shortcomings in terms of predicting the detailed behavior such as critical exponents, the van der Waals equation of state provides a simple description of the qualitative behavior of a fluid near its critical point. The van der Waals equation of state is given by

$$\left(p + \frac{9RT_c}{8\rho_c}\rho^2\right)\left(1 - \frac{\rho}{3\rho_c}\right) = \rho RT, \tag{9}$$

where R is the universal gas constant, ρ_c is the critical density and T_c is the critical temperature.

If we use equation (7) to write the van der Waals equation of state (9) in terms of a free energy, we find that it has a double-well structure below T_c and a single-well structure above T_c. We shall assume a free energy per unit volume of the general form

$$\rho f \;=\; \rho_c c_1(T) + \rho_c c_2(T)\left(\frac{\rho-\rho_c}{\rho_c}\right) + B_0\left[\frac{a^2}{2}\frac{T-T_c}{T_c}\left(\frac{\rho-\rho_c}{\rho_c}\right)^2 + \frac{1}{4}\left(\frac{\rho-\rho_c}{\rho_c}\right)^4\right], \tag{10}$$

where $c_1(T)$ is a temperature-dependent integration constant whose form is not determined by the van der Waals equation of state (9) and $c_2(T)$ is related to $c_1(T)$. The determination of $c_1(T)$ requires an additional thermal equation of state (e.g. see Callen [51]). Also, the parameters B_0 and a^2 are treated as adjustable. This reduces to the van der Waals form, expanded locally near the critical temperature and density, when $B_0 = \frac{9}{16}\rho_c RT_C$ and $a^2 = 4$. Equations (8) and (10) lead to the dimensionless equation for the static density profile

$$\tilde{\epsilon}^2\frac{d^2\tilde{\rho}}{d\tilde{z}^2} = \tilde{g}\tilde{z} + a^2\tilde{T}\tilde{\rho} + \tilde{\rho}^3 \tag{11}$$

where $\tilde{\rho} = (\rho - \rho_c)/\rho_c$, $\tilde{T} = (T - T_c)/T_c$, $\tilde{z} = z/L$, $\tilde{\epsilon}^2 = K\rho_c^2/B_0L^2$ and $\tilde{g} = \rho_c gL/B_0$. We have taken $\rho = \rho_c$ at $z = 0$. An approximate analytical solution to equation (11) can be obtained in the limit $\tilde{\epsilon} \ll 1$. For $\tilde{T} < 0$ (i.e. two-phase region) and $\tilde{z} < 0$, we use the method of matched asymptotic expansions to obtain

$$\tilde{\rho} = \tilde{\rho}_{out} - a\sqrt{-\tilde{T}}\tanh\left(\frac{a\sqrt{-\tilde{T}}\tilde{z}}{\sqrt{2}\tilde{\epsilon}}\right) - a\sqrt{-\tilde{T}} + \ldots, \tag{12}$$

where $\tilde{\rho}_{out}$ corresponds to the root of the equation $0 = \tilde{g}\tilde{z} + a^2\tilde{T}\tilde{\rho} + \tilde{\rho}^3$ that has $\tilde{\rho} > a\sqrt{-\tilde{T}}$. For $\tilde{T} > 0$ (i.e. one-phase region) we can express the solution in terms of the regular expansion

$$\tilde{\rho} = \tilde{\rho}_0 + \frac{6\tilde{\epsilon}^2\tilde{g}^2\tilde{\rho}_0}{(a^2\tilde{T} + 3\tilde{\rho}_0^2)^4} + \ldots, \tag{13}$$

where $\tilde{\rho}_0$ is the real root of $0 = \tilde{g}\tilde{z} + a^2\tilde{T}\tilde{\rho}_0 + \tilde{\rho}_0^3$. The density profiles are antisymmetric about $\tilde{z} = 0$. Using equations (10), (7) and $s = -f_T$ we can compute expressions for the basic-state pressure $p_0(z)$ and entropy $s_0(z)$. Note that the entropy $s_0(z)$ depends on $c_1(T)$. Further details of this are discussed in section 5; for now we note that specification of $s_0(z)$ is not necessary for the development that follows.

Static density profiles are shown in figure 2 for temperatures both above and below the critical temperature. The parameter values used to calculate these profiles are $\epsilon_{DL} = 10^{-4}$, $a = 4.85$ and $\tilde{g} = 1.631 \times 10^{-4}$ where $\epsilon_{DL}^2 = \tilde{\epsilon}^2/\tilde{g}$. The parameters a^2 and $\tilde{g}$ were chosen to fit as closely as possible the density profiles shown in Berg *et al.* far above the critical temperature (see their figure 1). The dashed curve corresponds to the density profile at the critical temperature. Above the critical temperature, there is a single stratified phase. Below the critical temperature, the fluid separates into two stratified phases. Again, we point out that while these profiles do not embody the quantitative behavior in terms of critical exponents, they do capture the qualitative behavior of the density near the critical point.

It is interesting to note that there is a significant amount of stratification which occurs over a relatively small length scale. While this stratification often plagues those seeking to make precise measurements of physical quantities of near-critical fluids such as xenon, it can also be seen as a unique feature through which phenomena that normally occur on much larger length scales, such as those common in oceanography or atmospheric sciences, can be studied in the laboratory.

3.2 Internal Wave Frequencies

We follow the analysis of Berg *et al.* [4] and seek neutrally stable wave modes by introducing perturbations to the basic-state solution as follows

$$\rho = \rho_0(z) + \hat{\rho}(z)\cos(q_x x)\cos(q_y y)e^{i\omega t}, \tag{14a}$$

$$u = 0 + \hat{u}(z)\sin(q_x x)\cos(q_y y)e^{i\omega t}, \tag{14b}$$

$$v = 0 + \hat{v}(z)\cos(q_x x)\sin(q_y y)e^{i\omega t}, \tag{14c}$$

$$w = 0 + \hat{w}(z)\cos(q_x x)\cos(q_y y)e^{i\omega t}, \tag{14d}$$

$$p = p_0(z) + \hat{p}(z)\cos(q_x x)\cos(q_y y)e^{i\omega t}, \tag{14e}$$

$$s = s_0(z) + \hat{s}(z)\cos(q_x x)\cos(q_y y)e^{i\omega t}, \tag{14f}$$

where $q_x = \pi j/a_x$ and $q_y = \pi k/a_y$ are the wavenumbers in the two horizontal directions with integer values for j and k and ω is the frequency. Note that we are interested in natural wave modes confined to the box and therefore have a discrete rather than continuous set of wave vectors. In fact, the modes we describe below have $j = k = 1$. The form for the velocity components has been chosen to allow $\vec{u}\cdot\hat{n} = 0$ on each wall.

As a simplification, we shall consider incompressible perturbations. In physical terms, this means that the response of a fluid parcel to a vertical perturbation is associated with changes in the background density gradient rather with any further compression of the parcel. That is, although the basic-state density profile develops as a result of the large compressibility of the fluid near its critical point, acoustic waves do not interact strongly with internal gravity waves. This can be put in more quantitative terms if we consider the Brunt-Väisälä frequency

$$N_{BV}^2 = -\frac{g}{\rho}\frac{\partial\rho}{\partial z} - \frac{g^2}{c^2}, \tag{15}$$

where c is the acoustic sound speed. This quantity measures the fluid's oscillatory response to stratification and compression [52]. Berg *et al.* argued that for the near-critical xenon system under consideration, the Brunt-Väisälä frequency could be approximated by the stratification term alone. This was based on a direct comparison for xenon of the first and second terms in equation (15). Since we expect that our density profiles approximate theirs in the bulk regions and that in the interfacial layer the density gradients used here may be quite large, we anticipate that this is a reasonable approximation to pursue. This can be stated more formally in terms of incompressible perturbations if we consider the equation of state $p = p(s, \rho)$. It follows that

$$\frac{Dp}{Dt} = \left.\frac{\partial p}{\partial s}\right|_{\rho} \frac{Ds}{Dt} + \left.\frac{\partial p}{\partial \rho}\right|_{s} \frac{D\rho}{Dt} = c^2 \frac{D\rho}{Dt}, \tag{16}$$

where $c^2 = \partial p/\partial \rho$ is the (adiabatic) sound speed and we have used $Ds/Dt = 0$. Since the basic state has no flow and varies only in the vertical direction we can reduce this to a statement about the perturbed quantities (denoted by primes)

$$\left(\frac{\partial \rho^{'}}{\partial t} + w^{'} \frac{d\rho_0}{dz} \right) = \frac{1}{c^2} \left(\frac{\partial p^{'}}{\partial t} + w^{'} \frac{dp_0}{dz} \right). \tag{17}$$

In terms of dimensionless quantities, the condition $Lg/c^2 \ll 1$ reveals at leading order the condition of incompressible perturbations $\partial \rho^{'}/\partial t + w^{'} d\rho_0/dz = 0$, or $\nabla \cdot \vec{u}^{'} = 0$ using (1a).

We insert expansions (14) into the governing equations (1), use the condition of incompressible perturbations, linearize, and find that

$$\begin{aligned}
i\omega\hat{\rho} + \hat{w}\frac{d\rho_0}{dz} &= 0, && (18a)\\
q_x\hat{u} + q_y\hat{v} + \frac{d\hat{w}}{dz} &= 0, && (18b)\\
i\omega\rho_0\hat{u} - q_x\hat{p} &= K\rho_0 q_x \left(q^2\hat{\rho} - \frac{d^2\hat{\rho}}{dz^2} \right), && (18c)\\
i\omega\rho_0\hat{v} - q_y\hat{p} &= K\rho_0 q_y \left(q^2\hat{\rho} - \frac{d^2\hat{\rho}}{dz^2} \right), && (18d)\\
i\omega\rho_0\hat{w} + \frac{d\hat{p}}{dz} &= -\hat{\rho}g + K\rho_0 \left(-q^2\frac{d\hat{\rho}}{dz} + \frac{d^3\hat{\rho}}{dz^3} \right) + K\hat{\rho}\frac{d^3\rho_0}{dz^3}, && (18e)
\end{aligned}$$

where $q^2 = q_x^2 + q_y^2$. Note that by virtue of the incompressible perturbation assumption, the equation for entropy s decouples and is not needed to compute the frequency. These equations can be combined to obtain the single perturbation equation

$$\left[1 - \frac{q^2}{\omega^2} M^2 \right] \frac{d^2\hat{w}}{dz^2} - \left[\frac{N^2}{g} + \frac{q^2}{\omega^2}\frac{1}{\rho_0}\frac{d(\rho_0 M^2)}{dz} \right] \frac{d\hat{w}}{dz} - q^2 \left[1 - \frac{N^2}{\omega^2} - \frac{q^2}{\omega^2} M^2 \right] \hat{w} = 0, \tag{19}$$

where

$$N^2 = -\frac{g}{\rho_0}\frac{d\rho_0}{dz}, \tag{20a}$$

$$M^2 = \frac{K}{\rho_0}\left(\frac{d\rho_0}{dz}\right)^2. \tag{20b}$$

The boundary conditions are that the vertical component of the velocity vanishes on the upper and lower boundaries $\hat{w}(L) = \hat{w}(-L) = 0$. This is an eigenvalue problem where the eigenvalue is the frequency ω and the eigenfunction $\hat{w}$ characterizes the wave mode.

It is of particular interest to note that this is a second-order system. The model used by Berg *et al.* for the single-phase region, which is also second-order, can be obtained by taking $K = 0$ (i.e. $M^2 = 0$) in equation (19). That is, the inclusion of the nonclassical terms in the incompressible limit does not result in a higher-order differential equation relative to that obtained for the classical model. However, we note here (and show later) that if we include the effects of compressible perturbations the result is a set of two coupled second-order equations. We present those equations and discuss them in more detail in section 5.

We have solved the eigenvalue problem (19) using a method given by Keller [53] whereby we replace one of the homogeneous boundary conditions with an independent inhomogeneous one. The integration of the resulting inhomogeneous boundary value problem was done using SUPORT [54]. This code uses a superposition of linearly-independent solutions coupled with an orthonormalization procedure to maintain their (numerical) independence. The integrations were performed using either an Adams-type method or a Runge-Kutta method. The eigenvalue ω and eigenfunction $\hat{w}(z)$ which satisfy the original homogeneous boundary condition were then obtained iteratively.

Figure 3 shows the internal wave frequencies obtained experimentally (solid points) and theoretically using the restricted cubic model (dashed curves) by Berg *et al.* and the theoretical predictions of the present diffuse-interface approach using the van der Waals model (solid curves). The parameter values used for the diffuse-interface calculations are $\epsilon_{DL} = 10^{-4}$, $a = 4.85$ and $\tilde{g} = 1.631 \times 10^{-4}$. The value of ϵ_{DL} used here was chosen to be well within the convergence region (with respect to the internal wave frequencies) shown in figure 4.

Figure 4 shows the dependence of the frequency on the parameter ϵ_{DL}. The solid curves correspond to the upper and lower modes at $T = T_c - 2.8972$ mK and the dashed curves correspond to the upper and lower modes at $T = T_c + 75.3272$ mK. For these temperatures, the results are converged for values of ϵ_{DL} smaller than 10^{-1} or 10^{-2}. The most significant departure from the converged value occurs for the lower mode and $T < T_c$ and indicates that the results can become very sensitive to values of ϵ_{DL} greater than 10^{-2}.

There are a number of comparisons that can be made between the theoretical results predicted with the single diffuse-interface model and those obtained by Berg *et al.* using two separate models. While by design, the diffuse-interface model agrees with the Berg *et al.* theory for temperatures well above the critical temperature (recall that the parameters in the present equation of state were chosen so that the density profile matches that of the Berg *et al.* theory well above the critical temperature), the difference becomes more pronounced as the temperature is decreased. As we shall see below and in the next figure, this difference can be attributed in full to the difference between the two equations of state used in the two models. That is, the diffuse-interface results differ from those of Berg *et al.* because the variation with temperature of the density profiles obtained with the van der Waals equation of state used here does not precisely match that of the density profiles obtained using the restricted cubic model. This may have important consequences in other studies using diffuse-interface models and an equation of state similar to the van der Waals model used here (for example, full numerical simulations of the governing equations). The present study gives an indication of how the equation of state affects the results. Another result of the diffuse-interface model is the premature termination of the frequency curves below the critical temperature. As we shall see below, this is the result of a breakdown of the disturbance equation (19) as the coefficient of the term $d^2\hat{w}/dz^2$ vanishes.

Figure 5 shows a comparison of the frequency computed using the single diffuse-interface model and that computed using the two separate models of Berg *et al.*, where *in each case* the equation of state (10) is used. Again the solid curves show the diffuse-interface results (with the same parameter values as shown in figure 3) and the dashed curves show the classical results. This comparison shows that with the exception of the regions below the critical temperature where the disturbance equation breaks down (see below), the diffuse-interface results reproduce the classical results. This indicates that it is the use of the simpler equation of state (10) in the present model, rather than an inherent difference between the diffuse and sharp-interface models, which accounts for the differences between the theoretical predictions shown in figure 3.

The disturbance equation (19) is a second-order equation whose leading coefficient $1 - q^2M^2/\omega^2$, as noted, may vanish. Although this coefficient depends on the vertical coordinate, we can estimate the point at which it first vanishes by evaluating it at $\tilde{z} = 0$, where the density gradient, and hence M, is largest. In terms of the frequency $\Omega = \omega/2\pi$ (in Hz) and temperature T this boundary is given by

$$\frac{\Omega}{\sqrt{g/L}} = \frac{(qL)a^2}{2\pi\sqrt{2\tilde{g}}}\left|\frac{T - T_c}{T_c}\right|. \tag{21}$$

Note that this result does not depend on the thickness of the interface. We have plotted this boundary in figure 5 (dashed-dotted line) for the parameter values as given above. This boundary is consistent with the points at which we can no longer compute numerical solutions to the present model (i.e. where the solid curves terminate in figures 3 and 5).

4. Discussion

In this section we discuss several of the issues raised by the above described analysis and numerical results. In particular we shall address possible improvements in terms of the equation of state used in the diffuse-interface model and also the issue of the limitations of the incompressible perturbation assumption.

The advantage of the equation of state employed in the present analysis is that from both a physical and mathematical viewpoint it is the simplest characterization of the near-critical behavior. An equation of state similar to this is typically chosen for numerical simulations of the full set of equations. The disadvantage, as we have seen, is that it does not provide as accurate of a representation of the density profiles as does the restricted cubic model, for example. One improvement that can be made is to use a modified van der Waals equation of state (e.g. Rowlinson and Widom [11], Fisk and Widom [55]). The modified van der Waals equation of state improves on the predictions in terms of critical exponents relative to the van der Waals equation of state but still allows an analytical solution for the density profiles.

The numerical solution and analysis of the disturbance equation (19) showed that its leading coefficient can vanish. This indicates the presence of a singularity. A key assumption used to derive this equation was that the perturbations were incompressible. Although we have used a simple equation of state and have used approximate techniques to write down the basic-state density profile, it seems quite clear that a more accurate representation of the density profile shall ultimately suffer the same consequences. In order to further understand this singularity, we shall rederive the disturbance equations without making the assumption of incompressibility. Using the same approach as described in section 3.2, we find that the disturbance equations that retain the effects of compressibility are given by

$$A_1\hat{p} + A_2\frac{d\hat{p}}{dz} + A_3\frac{d^2\hat{p}}{dz^2} + A_4\hat{q} + A_5\frac{d\hat{q}}{dz} + A_6\frac{d^2\hat{q}}{dz^2} = 0, \tag{22a}$$

$$B_1\hat{p} + B_2\frac{d\hat{p}}{dz} + B_4\hat{q} + B_5\frac{d\hat{q}}{dz} + B_6\frac{d^2\hat{q}}{dz^2} = 0, \tag{22b}$$

where $\hat{q} = \rho_0\hat{w}$ and the (variable) coefficients A_i and B_i are given in Appendix A.

These are two coupled second-order equations describing a 'diffuse/compressible' flow. It is of interest to recover several lower-order cases from this system; that is, the 'diffuse/incompressible', 'classical/compressible' and 'classical/incompressible' cases.

The 'diffuse/incompressible' case can be obtained formally by setting $1/c^2(z) = 0$ in the expressions in Appendix A. In this case, the coefficients A_2, A_3 and B_2 all vanish. It can then be easily seen that equations (22) reduce to a second-order equation for $\hat{q}$, or equivalently, for $\hat{w}$ (see equation (19)). Therefore, in the context of the diffuse-interface formulation, the incompressible limit is singular.

This is in contrast to the classical case, as can be seen if we compare the 'classical/compressible' and 'classical/incompressible' cases. First, to obtain the classical (single-phase) description from equations (22) we take $K = 0$. Here, the coefficients A_2, A_3 and A_6 vanish. It is again easy to see that the resulting coupled equations for $\hat{p}$ and $\hat{q}$ can be reduced to a second-order equation for $\hat{q}$. This represents the 'classical/compressible' case. In the 'classical/incompressible' case, which again we can obtain by further setting $1/c^2(z) = 0$, we find that the coefficient B_2 vanishes. Therefore, in the classical case, the disturbance equations are second-order regardless of whether or not the effects of compressibility are included. The above description shows that the limit of incompressible perturbations is a regular limit in the classical formulation but is a singular limit in the diffuse-interface formulation.

In order to solve equations (22), the sound speed must first be specified. This, however, cannot be calculated from the classical van der Waals equation of state alone. A thermal equation of state, consistent with the van der Waals equation, must be given [51].

For the present purposes, we would like only to confirm that the inclusion of the terms due to compressibility relieve the singularity observed in the incompressible calculations and allow us to calculate frequencies at lower temperatures. Therefore, we shall not be concerned with the specific form used for the sound speed. In the single-phase region, we have used the 'linear model' as given by Hohenberg and Barmatz [2] to compute the sound speed. Note that this model is used to compute the sound speed only; we still use the van der Waals equation of state to compute the density profiles. Our calculations show that the inclusion of compressibility effects in the one-phase region lead to negligible corrections in terms of the resulting internal wave frequencies. This is to be expected based on the fact that our incompressible calculations encountered no difficulty in the one-phase region. That is, the inclusion of compressibility in the one-phase region represents a regular perturbation. This reinforces the statements given by Berg *et al.* [4] who argued that the compressibility effects should be negligible with respect to the internal gravity wave frequency predictions. The above described 'linear model' applies in the classical sense below the critical point, in that it can be used to calculate the sound speed on either side of a sharp interface. However, there is no rigorous way of connecting the two profiles through the diffuse-interface used in the present calculations. Therefore, in the two-phase region we have used a constant value for the sound speed in order to solve the eigenvalue problem. Although this *ad hoc* prescription for the sound speed does not provide an accurate approximation to the true sound speed, which can vary significantly in the vertical direction, it is sufficient for our purposes in that it is nonzero everywhere and can be made to represent the true sound speed in an average sense. We have found that this approach does in fact allow us to calculate internal wave frequencies beyond the line of singularity shown in figure 5. Therefore, we can conclude that the effects of compressibility relieve this singularity and may not be negligible when using the diffuse-interface formulation as we have presented here.

As an additional check, we have calculated the solutions for the case where the capillarity terms are included in the basic-state density profile while the terms involving M^2 and its derivatives are ignored in an *ad hoc* way in equation (19). From the point of view of the perturbation equation, the system behaves as if it were in a single phase, with the density profile represented as before in both the one-phase and two-phase regions. The results of this calculation are graphically identical to the dashed curves shown in figure 5, which represent the sharp-interface model results. Unlike the full incompressible case where the capillary terms M^2 are included in the perturbation equation (19), these calculations are not limited by the line of singularity.

5. Conclusions

We have used a diffuse-interface model to describe internal gravity waves in near-critical xenon. This analysis extends that of Berg *et al.* [4], who studied the problem experimentally and theoretically using separate hydrodynamic descriptions above and below the critical temperature. The present diffuse-interface description of the hydrodynamics can be used to calculate the internal wave frequencies both above and below the critical temperature. We have studied the sensitivity of the model to the value of the gradient energy coefficient. For sufficiently small values of the gradient energy coefficient, the single diffuse-interface model recovers the classical results when the same equation of state is used in each case.

An unexpected result identified here is that the incompressible flow limit is singular in the context of the diffuse-interface limit. That is, when the effects of compressibility are neglected, the internal wave problem is governed by a second-order perturbation equation, but when the effects of compressibility are included, the problem is governed by a system of two second-order perturbation equations. This is in contrast to the classical case where the limit of incompressibility is regular.

Acknowledgements

The authors would like to acknowledge support by the National Aeronautics and Space Administration Microgravity Science and Applications Program. One of the authors (D.M.A.) acknowledges the support of a National Research Council Postdoctoral Fellowship. The authors would like to thank L.K. Antanovskii, R.F. Berg, S.R. Coriell, J. Lowengrub, M.J. Lyell, B.T. Murray, R.L. Pego, R.G. Rehm, R.F. Sekerka, M. Shelley and A.A. Wheeler, and the editor for helpful discussions.

Appendix A. Coefficients of Compressible Equations

The following are the coefficients appearing in the compressible perturbation equations (22).

$$A_1 = \frac{1}{i\omega}\left[q^2 - \frac{\omega^2}{c^2(z)} + Kq^2\rho_0\left(\frac{q^2}{c^2(z)} - \left(\frac{1}{c^2(z)}\right)''\right)\right], \tag{A1a}$$

$$A_2 = -\frac{2Kq^2}{i\omega}\rho_0\left(\frac{1}{c^2(z)}\right)', \tag{A1b}$$

$$A_3 = -\frac{Kq^2}{i\omega}\frac{\rho_0}{c^2(z)}, \tag{A1c}$$

$$A_4 = \frac{N_K(z)}{g} - \frac{Kq^4}{g\omega^2}\rho_0 N_K(z) + \frac{Kq^2}{g\omega^2}\rho_0 N_K''(z), \tag{A1d}$$

$$
\begin{aligned}
A_5 &= 1 + \frac{2Kq^2}{g\omega^2}\rho_0 N_K^{'}(z), &\text{(A1e)}\\
A_6 &= \frac{Kq^2}{g\omega^2}\rho_0 N_K(z), &\text{(A1f)}\\
B_1 &= \frac{1}{i\omega}\left[\frac{1}{\rho_0^2}\frac{d\rho_0}{dz} + \frac{\omega^2}{q^2}\left(\frac{1}{\rho_0 c^2(z)}\right)^{'} + \frac{g}{\rho_0 c^2(z)} - \frac{K}{\rho_0 c^2(z)}\frac{d^3\rho_0}{dz^3}\right], &\text{(A1g)}\\
B_2 &= \frac{1}{i\omega}\left[\frac{\omega^2}{q^2\rho_0 c^2(z)}\right], &\text{(A1h)}\\
B_4 &= -\frac{1}{gq^2}\left(\frac{N_K(z)}{\rho_0}\right)^{'} - \frac{N_K(z)}{\omega^2\rho_0} + \frac{1}{\rho_0} + \frac{K}{g\omega^2}\frac{N_K(z)}{\rho_0}\frac{d^3\rho_0}{dz^3}, &\text{(A1i)}\\
B_5 &= -\frac{N_K(z)}{gq^2\rho_0} + \frac{1}{q^2\rho_0^2}\frac{d\rho_0}{dz}, &\text{(A1j)}\\
B_6 &= -\frac{1}{q^2\rho_0}, &\text{(A1k)}
\end{aligned}
$$

where

$$
N_K(z) = -\frac{g}{\rho_0}\frac{d\rho_0}{dz} - \frac{g^2}{c^2(z)} + \frac{Kg}{c^2(z)}\frac{d^3\rho_0}{dz^3}. \tag{A2}
$$

References

[1] H.E. Stanley, *Introduction to Phase Transitions and Critical Phenomena* (Oxford University Press, Oxford, 1971).

[2] P.C. Hohenberg and M. Barmatz, "Gravity effects near the gas–liquid critical point," Phys. Rev. A **6**, 289 (1972).

[3] M.R. Moldover, J.V. Sengers, R.W. Gammon and R.J. Hocken, "Gravity effects in fluids near the gas–liquid critical point," Rev. Mod. Phys. **51**, 79 (1979).

[4] R.F. Berg, M.J. Lyell, G.B. McFadden and R.G. Rehm, "Internal waves in xenon near the critical point," Phys. Fluids **8**, 1464–1475 (1996).

[5] M.Sh. Giterman, "Study of the critical state of a liquid using gravitational waves," Sov. Phys. Dokl. **12**, 1141 (1968).

[6] V.D. Khait, "On gravitational waves in a gas near the critical point for the gas-liquid transition," Sov. Phys. JETP **30**, 177 (1970).

[7] M.Sh. Giterman and V. A. Shteinberg, "Internal gravitational waves and convective instability in liquids," Mekh. Zhi. Gosta **7**, 55 (1972); English translation in Fluid Dyn. **7**, 238 (1972).

[8] J.T. Ho and J.D. Litster, "Faraday Rotation near the Ferromagnetic Critical Temperature of $CrBr_3$," Phys. Rev. B **2**, 4523 (1970).

[9] J.W. Cahn and J.E. Hilliard, "Free Energy of a Nonuniform System. I. Interfacial Free Energy," J. Chem. Phys. **28**, 258 (1958).

[10] P.M. Chaikin and T.C. Lubensky, *Principles of Condensed Matter Physics* (Cambridge, New York, 1995).

[11] J.S. Rowlinson and B. Widom, *Molecular Theory of Capillarity* (Clarendon, Oxford, 1989).

[12] G. Caginalp, "Stefan and Hele-Shaw type models as asymptotic limits of the phase-field equations," Phys. Rev. A **39**, 5887 (1989).

[13] R. Kobayashi, "Modeling and numerical simulations of dendritic crystal growth," Physica D **63**, 410 (1993).

[14] S.-L. Wang, R.F. Sekerka, A.A. Wheeler, B.T. Murray, S.R. Coriell, R.J. Braun and G.B. McFadden, "Thermodynamically-consistent phase-field models for solidification," Physica D **69**, 189 (1993).

[15] A.A. Wheeler, B.T. Murray and R.J. Schaefer, "Computation of dendrites using a phase-field model," Physica D **66**, 243 (1993).

[16] R.J. Braun, G.B. McFadden and S.R. Coriell, "Morphological Instability in Phase-Field Models of Solidification," Phys. Rev. E **49**, 4336 (1994).

[17] J.A. Warren and W.J. Boettinger, "Prediction of dendritic growth and microsegregation patterns in a binary alloy using the phase-field method," Acta. metall. mater. **43**, 689 (1995).

[18] J.W. Cahn and S.M. Allen, "A microscopic theory for domain wall motion and its experimental verification in Fe-Al alloy domain growth kinetics," J. Phys. (Paris) Colloque C7, C7-51 (1977).

[19] R.J. Braun, J.W. Cahn, G.B. McFadden, and A.A. Wheeler, "Anisotropy of interfaces in an ordered alloy: a multiple-order-parameter model," Phil. Trans. Roy. Soc. (London), in press.

[20] M. Fixman, "Transport coefficients in the gas critical region," J. Chem. Phys. **47**, 2808–2818 (1967).

[21] B.U. Felderhof, "Dynamics of the diffuse gas-liquid interface near the critical point," Physica **48**, 541 (1970).

[22] K. Kawasaki, "Kinetic equations and time correlation functions of critical fluctuations," Ann. Phys. **61**, 1–56 (1970).

[23] J.S. Langer and L.A. Turski, "Hydrodynamic model of the condensation of a vapor near its critical point," Phys. Rev. A **8**, 3230 (1973).

[24] B.I. Halperin, P.C. Hohenberg and E.D. Siggia, "Renormalization-group calculations of divergent transport coefficients at critical points," Phys. Rev. Lett. **32**, 1289–1292 (1974).

[25] L. de Sobrino, "Some Thermodynamic and Stability Properties of a Fluid With Gradient Dependent Free Energy," Can J. Phys. **54**, 105–117 (1976).

[26] E.D. Siggia, B.I. Halperin and P.C. Hohenberg, "Renormalization-group treatment of the critical dynamics of the binary-fluid and gas-liquid transitions," Phys. Rev. B **13**, 2110–2123 (1976).

[27] P.C. Hohenberg and B.I. Halperin, "Theory of dynamic critical phenomena," Rev. Mod. Phys. **49**, 435–479 (1977).

[28] A. Onuki and K. Kawasaki, "Nonequilibrium steady state of critical fluids under shear flow: a renormalization group approach," Ann. Phys. **121**, 456–528 (1979).

[29] A. Onuki, K. Yamazaki and K. Kawasaki, "Light scattering by critical fluids under shear flow," Ann. Phys. **131**, 217–242 (1981).

[30] J.E. Dunn and J.B. Serrin, "On the Thermomechanics of Interstitial Working," Arch. Rat. Mech. **88**, 95 (1985).

[31] V.N. Starovoitov, "Model of the motion of a two-component liquid with allowance of capillary forces," J. Appl. Mech. Techn. Phys. **35**, 891–897 (1994).

[32] L.K. Antanovskii, "A phase-field model of capillarity," Phys. Fluids **7**, 747 (1995).

[33] M.E. Gurtin, D. Polignone and J. Viñals, "Two-phase binary fluids and immiscible fluids described by an order parameter," Mathematical Models and Methods in Applied Sciences, **6**, (1996).

[34] R. Chella and J. Viñals, "Mixing of a two-phase fluid by cavity flow," Phys. Rev. E **53**, 3832 (1996).

[35] D. Jasnow and J. Viñals, "Coarse-grained description of thermo-capillary flow," Phys. Fluids **8**, 660 (1996).

[36] D. Jacqmin, "An energy approach to the continuum surface tension method," in *Proceedings of the 34th Aerospace Sciences Meeting and Exhibit*, (American Institute of Aeronautics and Astronautics), Reno, 1996.

[37] P. Seppecher, "Moving contact lines in the Cahn–Hilliard theory," Int. J. Engng. Sci. **34**(9), 977–992 (1996).

[38] B.T. Nadiga and S. Zaleski, "Investigations of a Two-Phase Fluid Model," submitted to European J. of Mech. B: Fluids (1997).

[39] J. Lowengrub and L. Truskinovsky, "Cahn-Hilliard Fluids and Topological Transitions," submitted to Proc. Roy. Soc. London A (1997).

[40] J.U. Brackbill, D.B. Kothe and C. Zemach, "A continuum method for modeling surface tension," J. Comp. Phys. **100**, 335 (1992).

[41] S.O. Unverdi and G. Tryggvason, "A front-tracking method for viscous, incompressible, multi-fluid flows," J. Comp. Phys. **100**, 25–37 (1992).

[42] S.O. Unverdi and G. Tryggvason, "Computations of multi-fluid flows," Physica D **60**, 70–83 (1992).

[43] J.A. Sethian, *Level Set Methods* (Cambridge University Press, Cambridge, 1996).

[44] D.J. Korteweg, "Sur la forme que prennent les équations du mouvements des fluides si l'on tient compte des forces capillaires causées par des variations de densité considérables mais continues et sur la théorie de la capillarité dans l'hypothèse d'une variation continue de la densité," Arch. Néerl. Sci. Exactes Nat. Ser. II **6**, 1 (1901).

[45] H.T. Davis and L.E. Scriven, "Stress and Structure in Fluid Interfaces," Adv. Chem. Phys. **49**, 357 (1982).

[46] E.C. Aifantis and J.B. Serrin, "The Mechanical Theory of Fluid Interfaces and Maxwell's Rule," J. Colloid Int. Sci. **96**, 517 (1983).

[47] E.C. Aifantis and J.B. Serrin, "Equilibrium Solutions in the Mechanical Theory of Fluid Microstructures," J. Colloid Int. Sci. **96**, 530 (1983).

[48] J.W. Cahn, "Critical Point Wetting," J. Chem. Phys. **66**, 3667 (1977).

[49] A.A. Wheeler, G.B. McFadden, and W.J. Boettinger, "Phase-field model for solidification of a eutectic alloy," Proc. R. Soc. Lond. A **452**, 495 (1996).

[50] D.M. Anderson and G.B. McFadden, "A Diffuse-Interface Description of Fluid Systems," NISTIR 5887, National Institute of Standards and Technology, Gaithersburg, MD 20899 (August 1996).

[51] H.B. Callen, *Thermodynamics and an Introduction to Thermostatics* (Wiley, New York, 1985).

[52] J. Lighthill, *Waves in Fluids* (Cambridge University Press, Cambridge, 1978).

[53] H.B. Keller, Numerical Solution of Two Point Boundary Value Problems, Regional Conference Series in Applied Mathematics (SIAM, Philadelphia, 1976, Vol. 24).

[54] M.R. Scott and H.A. Watts, "Computational Solution of Linear Two-Point Boundary Value Problems Via Orthonormalization" SIAM J. Numer. Anal. **14**, 40–70 (1977).

[55] S. Fisk and B. Widom, "Structure and free energy of the interface between fluid phases in equilibrium near the critical point," J. Chem. Phys. **50**, 3219–3227 (1969).

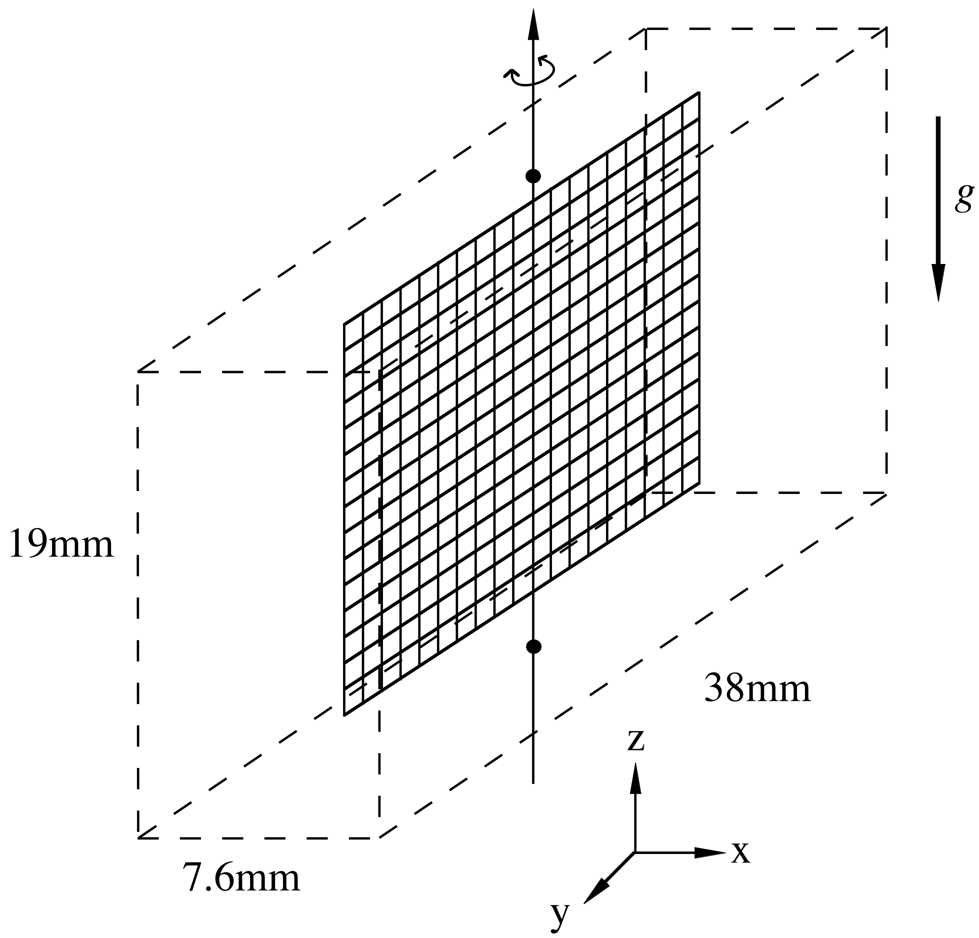

Figure 1: This figure shows the model configuration filled with a stratified fluid. The dimensions are $0 \leq x \leq a_x$, $0 \leq y \leq a_y$ and $-L \leq z \leq L$ where $a_x = 7.6$mm, $a_y = 38$mm and $L = 9.5$mm are the values corresponding to the experiment by Berg *et al.* The paddle, which in the experiments creates the initial disturbance, is shown for reference and is not present in the mathematical model.

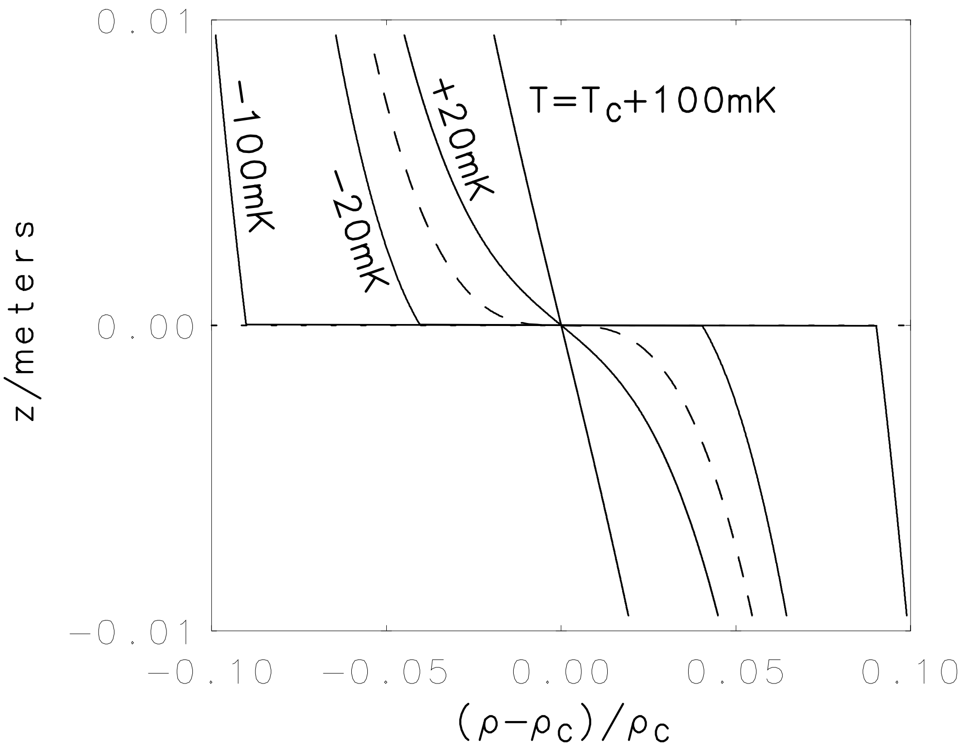

Figure 2: This figure shows the static density profiles representing solutions of equation (11). Each curve corresponds to a different temperature as indicated. The dashed curve corresponds to the density profile at the critical temperature. Above the critical temperature, there is a single stratified phase. Below the critical temperature, the fluid separates into two stratified phases. The parameter values used to calculate these profiles are $\epsilon_{DL} = 10^{-4}$, $a = 4.85$, $\tilde{g} = 1.631 \times 10^{-4}$.

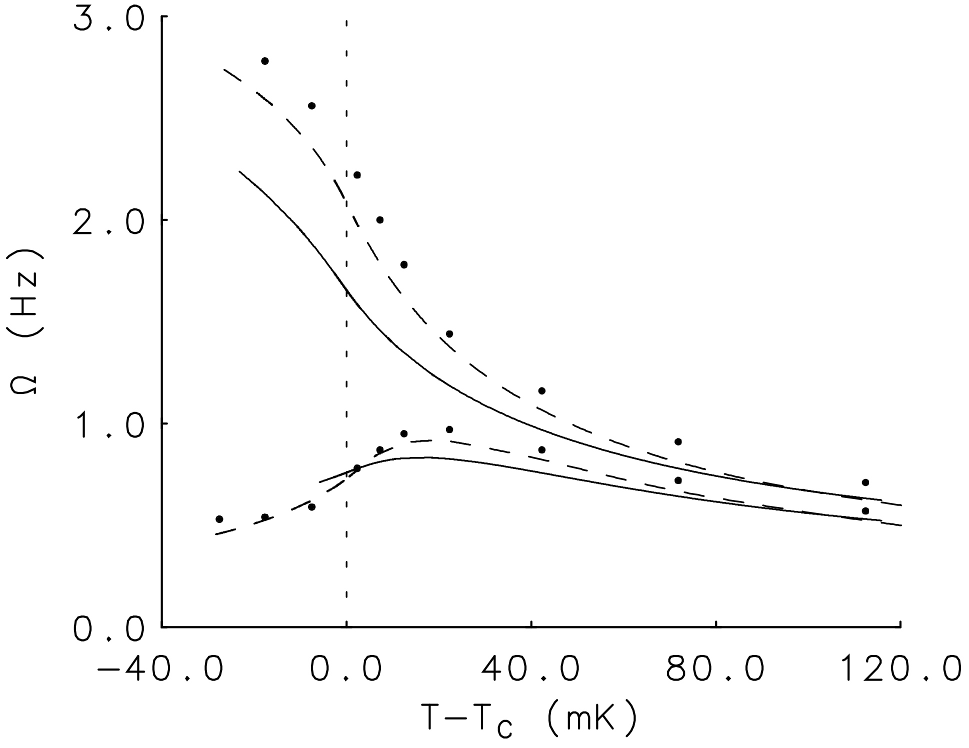

Figure 3: This figure shows the internal wave frequencies $\Omega = \omega/2\pi$ (in Hz) obtained experimentally by Berg *et al.* (data points), the theoretical predictions by Berg *et al.* (dashed curves) using two separate models above and below the critical temperature coupled with a restricted cubic model for the equation of state, and the theoretical predictions of the present diffuse-interface approach (solid curves) using a van der Waals equation of state. The vertical dashed line indicates the critical temperature. The parameter values used for the diffuse-interface calculations are $\epsilon_{DL} = 10^{-4}$, $a = 4.85$ and $\tilde{g} = 1.631 \times 10^{-4}$.

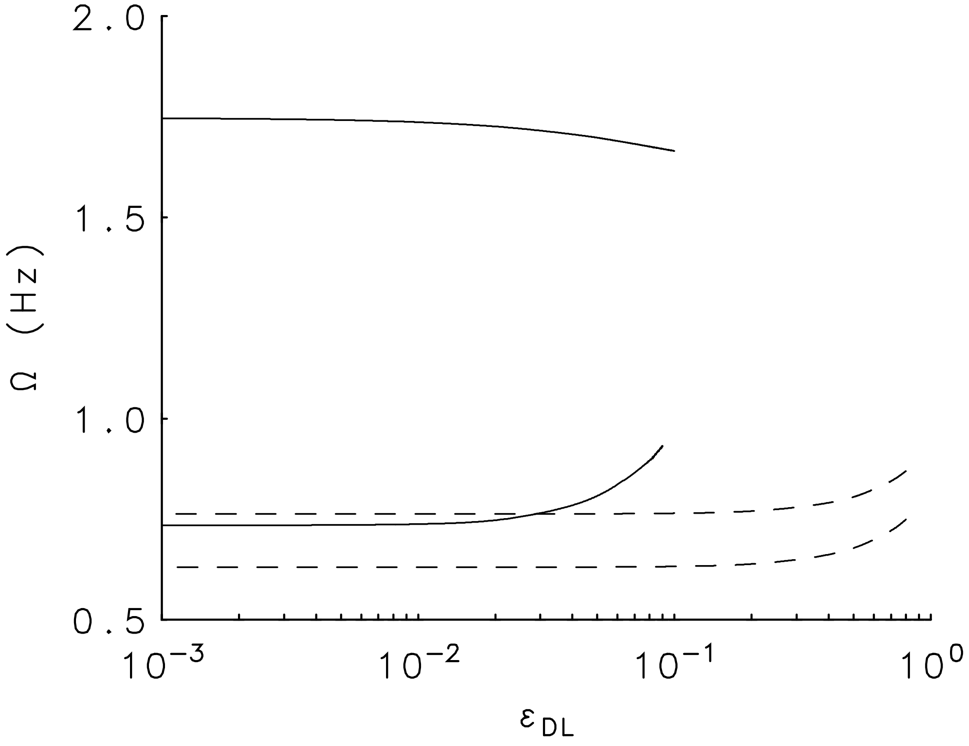

Figure 4: This figure shows the dependence of the internal wave frequencies on the parameter ϵ_{DL}. We have used $a = 4.85$ and $\tilde{g} = 1.631 \times 10^{-4}$. The solid curves correspond to the upper and lower modes for $T = T_c - 2.8972$ mK and the dashed curves correspond to the upper and lower modes for $T = T_c + 75.3272$ mK.

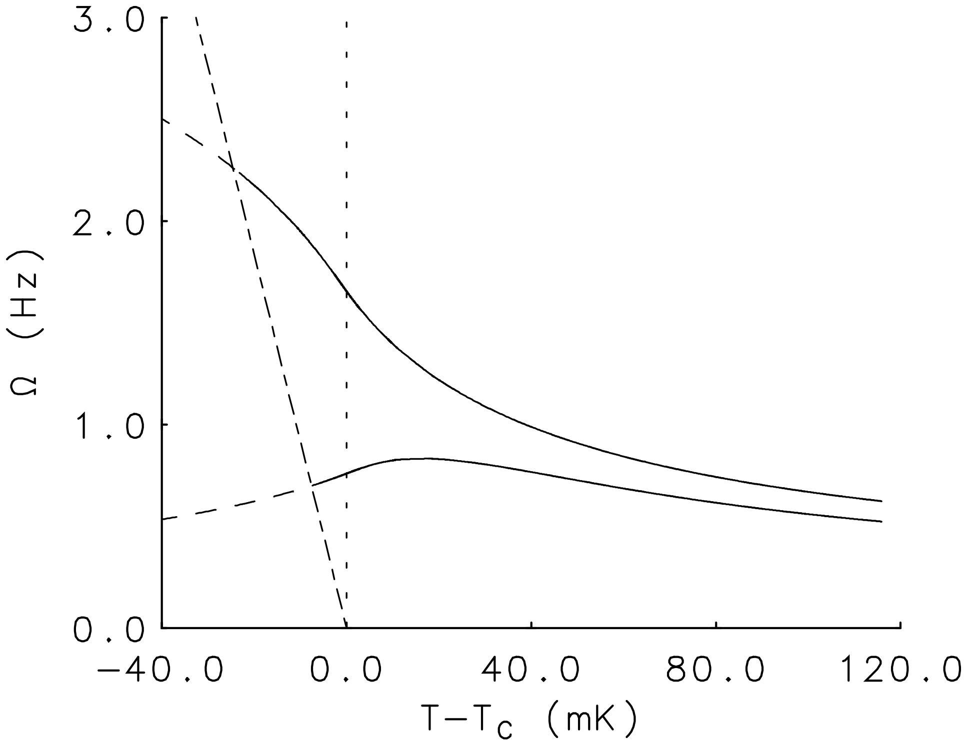

Figure 5: This figure shows a direct comparison of the frequency calculated using the classical model and that calculated with the diffuse-interface model. In each case we have used (10) as the equation of state. The vertical dashed line indicates the critical temperature. We find that in this case the diffuse-interface model (solid curves) recovers the classical model (dashed curves) given by Berg *et al.* The dashed-dotted line in this figure indicates the location where the coefficient $1 - q^2M^2/\omega^2$ of the second-order term in equation (19) is predicted to vanish, and hence indicates the boundary beyond which we cannot compute with the present model in the incompressible perturbation limit. Since this coefficient depends on the vertical coordinate, we have identified this boundary by evaluating the coefficient at $\tilde{z} = 0$, where the density gradient, and hence M, is greatest.